

Diffuse scattering and the mechanism for the phase transition in triglycine sulphate

J. M. Hudspeth · D. J. Goossens · T. R. Welberry ·
M. J. Gutmann

Received: 15 April 2013 / Accepted: 17 May 2013 / Published online: 31 May 2013
© Springer Science+Business Media New York 2013

Abstract Despite the order/disorder nature of its ferroelectric phase transition, and evidence for the evolution of local order as being important for understanding the transition, no comprehensive diffuse scattering study of the short-range order in triglycine sulphate, (TGS), $(\text{NH}_2\text{CH}_2\text{COOH})_3\text{H}_2\text{SO}_4$ has been undertaken. Diffuse scattering from single crystals is sensitive to two-body correlations, and can act as a probe of local structure, which in a second order phase transition acts as a precursor to the low temperature phase. The role of hydrogen bonding and dipolar interactions in the ferroelectric phase transition in TGS has been a long matter of conjecture. Using neutron and X-ray single crystal diffuse scattering this study shows that hydrogen bond mediated interactions between polarising glycine molecules cause local one-dimensional polarised domains to develop, oriented parallel to the b axis. These domains interact via dipolar interactions, and the three-dimensional ferroelectric order arises. This provides a real-space, interaction-based model for the phase transition in TGS, showing in detail how the local chemistry and physics give rise to the polarised state.

Introduction

Diffuse scattering from a crystalline material is the coherent scattered intensity that is not localised on the reciprocal lattice points. It comes about due to short-range order (SRO) in the crystal, and is sensitive to two-body correlations. Its analysis can determine details about the nature of the SRO in the crystal [32]. As systems undergo phase transitions from disorder to order (for example on cooling) the correlations between atoms and molecules grow, and eventually the correlation length diverges and a new phase is obtained. Hence, the study of the diffuse scattering from a system close to its phase transition(s) can shed light on the nature and mechanism of the transition [12].

Triglycine sulphate, (TGS), $(\text{NH}_2\text{CH}_2\text{COOH})_3\text{H}_2\text{SO}_4$, undergoes a ferroelectric phase transition at $T_C = 322$ K (49 °C) (~ 334 K in the case of fully deuterated TGS, FDTGS [15]), and the phase transition is of second-order, order-disorder type [11, 23]. Above T_C , in the paraelectric phase, one of the glycine molecules (labelled G1 in Fig. 1), and particularly the NH_3^+ group within it, is disordered across a mirror plane [3]. The G2 and G3 molecules are then equivalent and the structure has the space group symmetry $P2_1/m$. On cooling through T_C , the orientation of G1 goes from being disordered about the mirror plane to being long-range ordered, with all of the NH_3^+ groups on one side, and the mirror plane disappears. The ordered orientation of G1 molecules lowers the space group symmetry to $P2_1$ and produces a spontaneous polarisation along the ferroelectric b axis.

While, the hydrogen bonds are generally believed to play a significant role in the phase transition of hydrogen containing ferroelectrics [6, 17], the role of the hydrogen bonds in TGS is unclear. The role of the short hydrogen

J. M. Hudspeth
Research School of Physics and Engineering, The Australian
National University, Canberra, ACT 0200, Australia
e-mail: jessica.hudspeth@anu.edu.au

D. J. Goossens (✉) · T. R. Welberry
Research School of Chemistry, The Australian National
University, Canberra, ACT 0200, Australia
e-mail: goossens@rsc.anu.edu.au

M. J. Gutmann
ISIS Facility, Rutherford Appleton Laboratory, Chilton, Didcot,
Oxon, UK

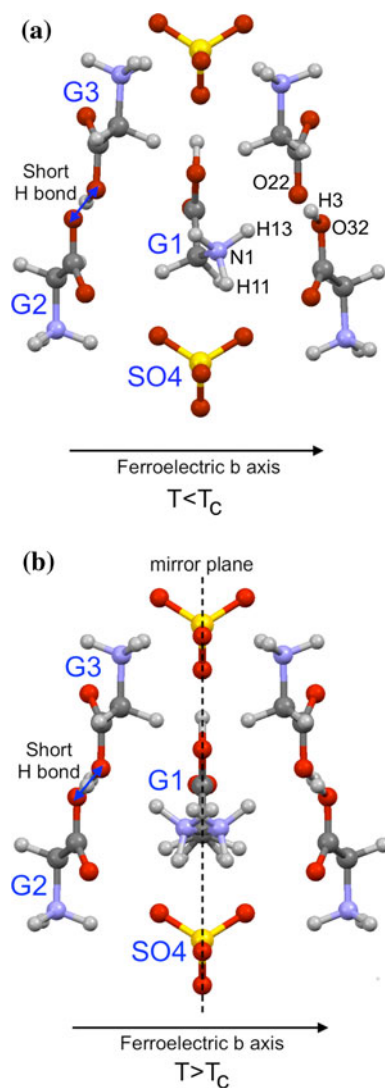


Fig. 1 Part of the unit cell of TGS in **a** the ferroelectric phase ($T < T_C$) and **b** the paraelectric phase ($T > T_C$)

bond between G2 and G3 is particularly poorly understood, with some studies suggesting that it may play a crucial role in triggering the phase transition [4, 14, 19], and others suggesting that it may not be involved [8, 9]. Kikuta et al. [21, 22] refined the structure of TGS with both positive and negative polarity by poling the crystal. They found that the position of the H3 atom in the G2–G3 bond is correlated with the G1 orientation. This supports the G2–G3 hydrogen bond being involved in the phase transition, although, it does not mean that it triggers it.

An argument against the G2–G3 hydrogen bond playing a dominant role in the phase transition is the fact that the increase in the phase transition temperature of TGS on deuteration is relatively small.

The change in the G2–G3 hydrogen bond geometry in TGS on deuteration is similar to that of the short hydrogen

bond in KDP [5], but the increase in T_C is only 12 K. This indicates that the G2–G3 short hydrogen bond is unlikely to be driving the transition. An alternative to the G2–G3 bond driving the phase transition is that the N1–D13···O22 and N1–D11···O3 hydrogen bonds (see Fig. 1) weakened with increasing temperature, allowing the G1 orientation to become disordered [16, 18].

It has been suggested that it is the dipole–dipole interactions between G1 molecules that drive the phase transition, rather than the hydrogen bonds. These interactions have been modelled in a number of ways. These include an Ising-type model, in which the pseudo Ising spin variables are the two orientational states of G1 along the ferroelectric b axis [10], and a unified oscillator model in which the NH_3^+ groups on G1 are considered to be interacting oscillators in a double-well potential [5, 6].

Critical diffuse scattering measurements show an anomalous rise in the diffuse scattering around some of the Bragg peaks in TGS for $T \sim T_C$ [10, 25, 29, 30]. The intensity of this critical diffuse scattering is a maximum at T_C and decreases with $|T - T_C|$; Further, its distribution is elongated perpendicular to b^* and narrow parallel to b^* , which suggested that the interactions between dipoles is strongest parallel to the ferroelectric b axis and that there are short-range correlations along b .

Here, analysis of X-ray and neutron diffuse scattering using Monte Carlo (MC) modelling is used to examine the SRO in TGS, and through that determine likely drivers for the phase transition. This is practicable because diffuse scattering is sensitive to two-body correlations [32], and therefore, allows us to explore the interactions between atoms and molecules.

Experimental

X-ray diffuse scattering

X-ray diffuse scattering data from TGS were collected on the 11-ID-B beamline at the Advanced Photon Source (APS) using the approach described in [34]. The crystal was mounted in front of a PerkinElmer amorphous silicon two-dimensional area detector. To collect a full three-dimensional volume of reciprocal space, the sample was rotated through 184° in ω with a step size of 0.25° . For each crystal orientation, 20×1 s exposures were recorded and summed together. A dark file (no beam) for the detector was collected every 4° .

The photon energy was 58.26 keV [$\lambda = 0.2127(1) \text{ \AA}$] and the size of the detector was 2048×2048 pixels, with a pixel size of $200 \times 200 \mu\text{m}$. The sample to detector distance was determined using a CeO_2 powder standard and

found to be 720.405 mm. This gave data out to a maximum q of approximately 8 \AA^{-1} .

Data were collected at 103, 223, 295, 322 (T_C), 373 and 423 K. The temperature was controlled using an Oxford Cryosystems Cryostream 700 Plus.

The program XCAVATE was used to reconstruct a three-dimensional volume of reciprocal space from the raw data and to extract two-dimensional slices of reciprocal space of interest [7, 26, 31, 34]. The $2/m$ Laue symmetry of the crystal was applied to generate data in the unrecorded regions, and to improve counting statistics in regions that were recorded more than once.

Neutron diffuse scattering

Neutron diffuse scattering data from FDTGS were measured on the SXD beamline at the ISIS spallation neutron source [20]. SXD combines the use of a time-of-flight measurement technique, and an array of 11 position-sensitive area detectors (covering a total of 49.4 % of the solid angle [20]) to access large volumes of reciprocal space for a given orientation of the crystal [20, 33]. Each detector has 64×64 pixels, with a pixel size of $3 \times 3 \text{ mm}$. For each neutron pulse, a time of flight spectrum is recorded for each pixel of each detector.

Close to full three-dimensional volumes of reciprocal space were obtained by recording diffuse scattering data at 6 different crystal orientations for each temperature. Data were collected at each crystal orientation until the integrated beam current reached $1500 \mu\text{A}$ ($\sim 10 \text{ h}$).

Data were collected at 300, 334 (T_C) and 373 K. The temperature was controlled using a closed-cycle refrigerator (CCR).

The raw data were processed using the program SXD2001 [20]. The reciprocal volume was calculated out to $q = 15 \text{ \AA}^{-1}$ with a step size of 0.1 \AA^{-1} and two-dimensional slices of reciprocal space were then extracted. The $2/m$ Laue symmetry of the crystal was applied to improve reciprocal space coverage.

Diffuse scattering data

Figure 2a shows neutron diffuse scattering in the $0 k l$ reciprocal layer of FDTGS, centred on the origin. These data were measured at 334 K ($T \sim T_C$). The Bragg peaks show irregular shapes due to the open geometry of the SXD instrument, which effectively images the crystal onto the detector. However, the intense neutron beam and large area detectors make the instrument very useful [33]. The most crucial features revealed in these data are the short streaks of scattering perpendicular to b^* ; Fig. 2b

shows these abstracted from (a). By taking further cuts at small increments of h (i.e. cuts parallel and close to $0 k l$) it can be shown that the streaks are cross sections through small pancake-like regions. This indicates that they are the results of small one-dimensional (1-d) domains parallel to b^* ; this shows good agreement with earlier results [10]; however, these more extensive data allow a model of the correlation structure of the polarising molecules.

This is especially true when X-ray diffuse scattering is incorporated, since the 11-ID-B beamline gave high-quality, low-noise data over a wide region of reciprocal space. As it is the NH_3^+ group that displaces most pronouncedly, and X-ray scattering is not sensitive to the H atoms, or D atom in the case of FDTGS, such data (see for example Fig. 3) is less sensitive to the polarised G1 molecule than is the neutron data, but shows thermal diffuse scattering very clearly, and does indeed show the domain-related streaking, although in fewer places (see Fig. 3b).

Although not as sensitive to the polarised G1 molecules, the high resolution of the X-ray data made it suitable for investigating the evolution of the diffuse streaks with temperature. Figure 3 shows part of the $0 k l$ slice of reciprocal space from the HTGS X-ray diffuse scattering data at 223, 322 ($T \sim T_C$), 373 and 423 K. The region around the (041) and (042) Bragg peaks is shown in more detail in Fig. 4, along with the plot profiles, measured in ImageJ [27], of the diffuse intensity between the peaks (Fig. 5).

Well below T_C , at 223 K (Fig. 3a) all the diffuse scattering intensity is thermal diffuse scattering, which is as expected since the system should be long-range ordered and all the G1 molecules in a given domain should have the same orientation. At 322 K, $T \sim T_C$ (Fig. 3b), the intensity of the thermal diffuse scattering is stronger than at 223 K,

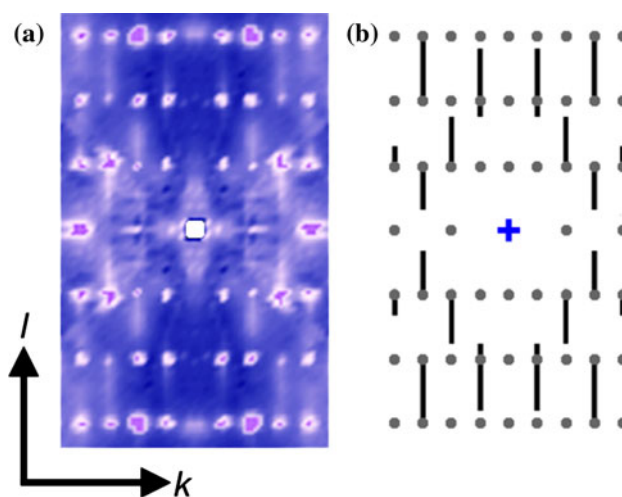


Fig. 2 The $0 k l$ slice of reciprocal space from the SXD neutron data at 334 K ($T \sim T_C$). **a** Shows a detailed view of the region in the centre of the slice, and **b** shows a schematic of the positions at which the diffuse streaks occur

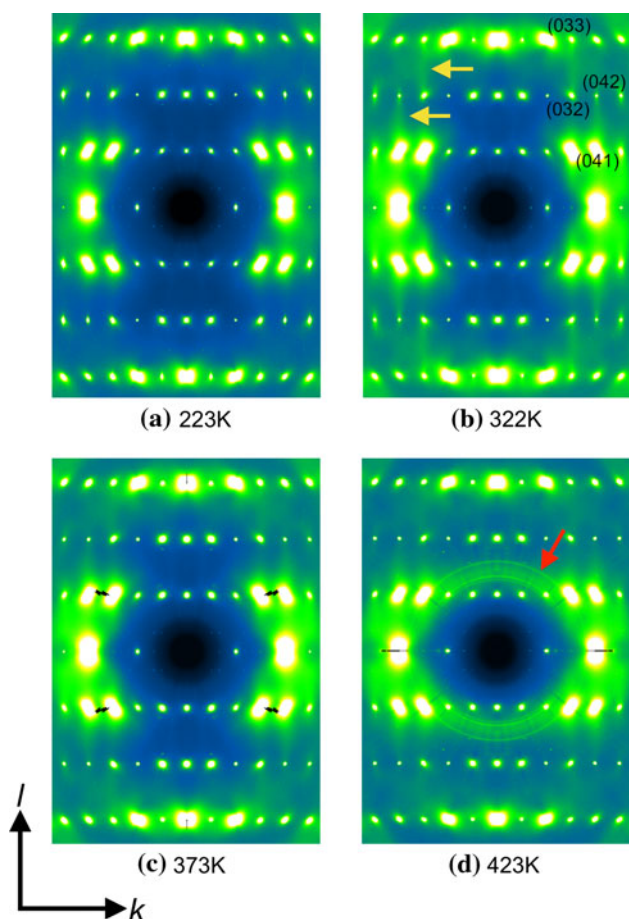


Fig. 3 Part of the $0\ k\ l$ slice of reciprocal space at **a** 223, **b** 322 ($T \sim T_C$), **c** 373 and **d** 423 K from the X-ray diffuse scattering data from HTGS. The positions of two of the diffuse streaks associated with the phase transition are indicated by the *yellow arrows* in **(b)**. The powder rings in the 423 K data, indicated by the *red arrow* in **(d)** were caused by the crystal starting to decompose, but did not affect the rest of the diffuse scattering pattern (Color figure online)

and the G1 SRO diffuse streaks perpendicular to the b^* (k) axis are clearly visible, as indicated in the figure. Above T_C , at 373 and 423 K (Fig. 3c, d), the streaks are still visible but appear weaker and more diffuse.

Although, the large temperature gaps between the measurements makes it impossible to determine exactly when the diffuse streaks (and therefore the onset of SRO) first occur, they most likely begin to appear between 40 and 30 K below T_C . No diffuse streaks were observed in the neutron data for FDTGS at 295 K ($T - T_C \approx 40$ K), but diffuse streaks were visible in the X-ray diffuse scattering from HTGS at 295 K ($T - T_C \approx 25$ K).

In order to gain a more quantitative understanding of the evolution of the diffuse streaks with temperature, the plot profiles of the intensities of the diffuse streak in the X-ray data between the (041) and (042) Bragg peaks were measured in ImageJ (Fig. 4e). It should be noted that no diffuse

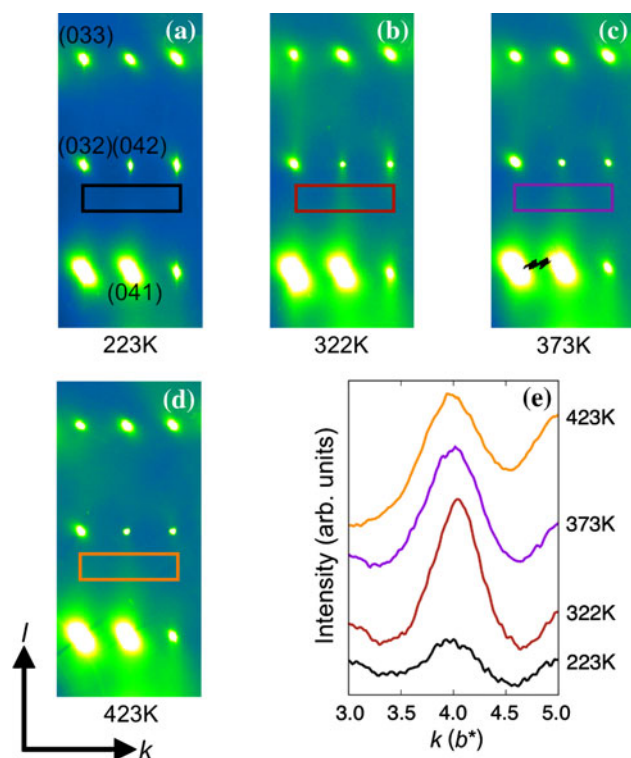


Fig. 4 The region around the (041) and (042) Bragg peaks in the $0\ k\ l$ slice of reciprocal space from the X-ray data at **a** 223, **b** 322 ($T \sim T_C$), **c** 373 and **d** 423 K. Plot profiles of the intensity in the region between the (041) and (042) Bragg peaks (indicated by the *rectangles*) are shown in **(e)**. The plot profiles were measured in ImageJ and have been vertically offset for clarity

streaks were observed in the 223 K data, so the small peak in the 223 K plot profile is most likely caused by the tail of the thermal diffuse scattering around the (041) Bragg peak. The plot profile at each temperature was fitted with a Gaussian.

Figure 5 shows that the FWHM decreases to a minimum at the phase transition temperature and then increases with increasing temperature. Similarly, the area increases to a maximum at the phase transition temperature and then decreases with increasing temperature. This indicates that the short-range correlations causing the diffuse streaks are strongest around the phase transition temperature and then weaken with increasing temperature.

Model description

For a two state system, occupancy can be described using a model analogous to the Ising model in magnetism [1, 24, 28]. The site occupancies are assigned a value of $S_i = \pm 1$, where $S = +1$ implies the NH_3^+ is displaced one way, and $S = -1$ implies it is displaced the other. If only nearest

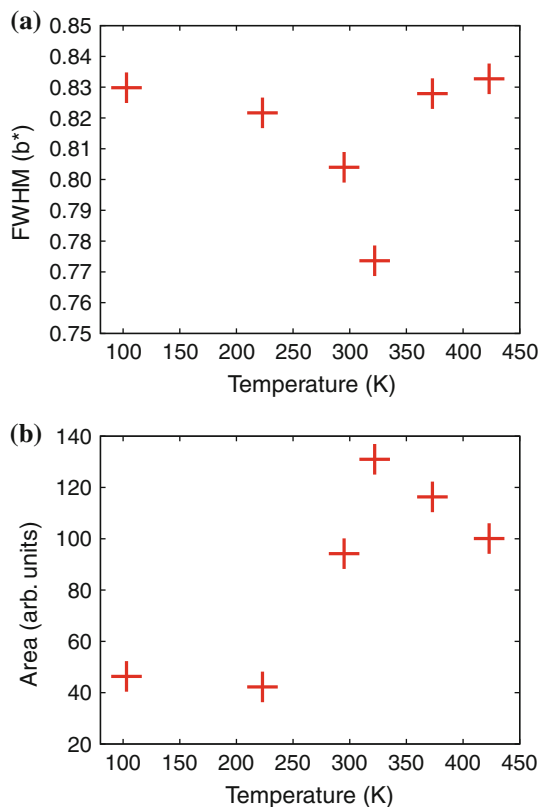


Fig. 5 The change in the FWHM and area with temperature of the diffuse streak between the (041) and (042) Bragg peaks observed in the $0\ k\ l$ slice of the X-ray data. The intensities of the peaks were measured using the plot profile tool in ImageJ, as shown in Fig. 4e, and fitted with a Gaussian

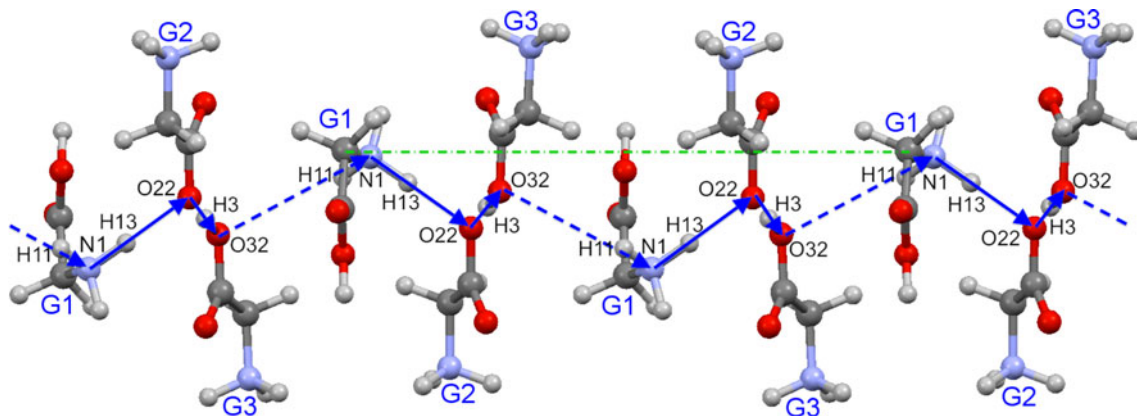


Fig. 6 Schematic of the ordering between b_1 first neighbour type G1 molecules being mediated by the short hydrogen bond between G2 and G3. Depending on the orientation of G1, the N1 atom can either be hydrogen bonded to O22 (as shown here) or to O32. If N1 is hydrogen bonded to O22 via N1–H13···O22 (indicated by the *solid arrows*), then H3 is covalently bonded with O32. This prevents the N1

neighbour (NN) interactions are considered, the energy of the spin is given by

$$E = \omega_{\text{NN}} \sum_{ij} S_i S_j \quad (1)$$

where ω_{NN} is the interaction constant and the sum is over NNs. The sign of ω_{NN} determines whether the occupancies tend to be positively or negatively correlated. In these simulations, a correlation magnitude was specified, and ω_{NN} was periodically adjusted to obtain the desired correlation. Once the correlation structure was generated, a model crystal of $32 \times 32 \times 32$ unit cells was constructed and its diffraction pattern calculated, using the program ZMC [13].

While, the principal correlation direction for the G1 molecules must clearly be parallel to the ferroelectric b axis, the G1 first neighbours directly along b (see the chain dotted line in Fig. 6), which is to say those G1 neighbours related by the full b unit cell vector, rather than the nearest G1 in the next cell along in b , are over 12 \AA apart. This distance is not unreasonable for dipole–dipole interactions, but is too large for there to be any direct intermolecular interactions.

Inspection of the average crystal structure suggests a mechanism, whereby, the molecules might be linked such that the G1 displacements will correlate as the data suggests. This is illustrated in Fig. 6. While the correlations appear to propagate along b , the interaction must be indirect. The short H-bond between G2 and G3 may act as

atom on the next G1 molecule from being able to form a hydrogen bond with O32 via N1–H11···O32 (indicated by the *dashed arrows*). This interaction propagates along the chain of b_1 first neighbours and leads to ordering of the G1 orientations. The chain *dotted line* indicates a direct G1 to G1 vector parallel to \mathbf{b}

intermediary, giving the zigzag network of interactions as illustrated (G1 pairs connected by these interactions are denoted to be of type *b1* to differentiate them from neighbours indirectly along *b*). Both correlations between *b1* type neighbouring G1 molecules and G1 molecules directly along *b* were tested in the MC modelling.

The diffuse scattering due to the G1 SRO will be modulated by the thermal motions of the molecules. This was modelled following a recently established approach [2].

Results and discussion

Figure 7 shows the calculated distribution of diffuse streaks in $0\ k\ l$ for a correlation coefficient (*cc*) of +0.95 between the *b1* neighbours (Fig. 7b) and between neighbours directly along *b* (Fig. 7c). The different correlation structures lead to significantly different distributions of the diffuse streaks in reciprocal space. The distribution extracted from the neutron data at 334 K is also shown for comparison purposes. No other disorder is present in the model, but it is clear that the diffuse streaks occur in the correct places for correlations between *b1* neighbours, whereas, the diffuse streaks for correlations between neighbours in *b* give a very poor match to the data.

The G1 orientations being correlated for *b1* first neighbour types suggests that the interactions are driven by the hydrogen bonds, rather than the dipole–dipole interactions since, as discussed above, the interactions between *b1* first

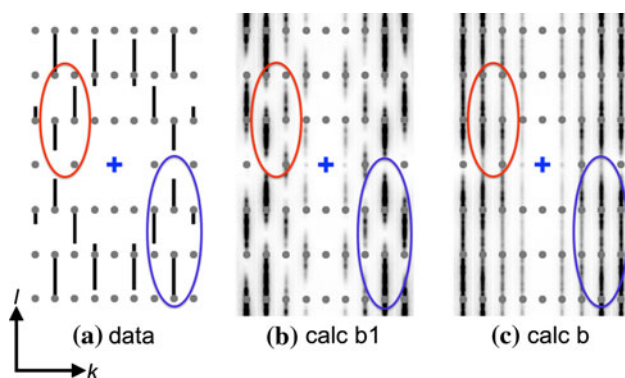


Fig. 7 The distribution of the diffuse streaks in the $0\ k\ l$ slice of reciprocal space **a** from the SXD neutron diffuse scattering data at 334 K (Fig. 2) and calculated from the orientational short-range order model with strong positive correlations ($cc \approx 0.95$) of the G1 orientations between **b** *b1* first neighbour types (zigzag chain as per Fig. 6), and **c** first neighbours directly along **b** (chain dotted line in Fig. 6). The positions of the Bragg peaks, indicated by the grey dots, have been superimposed on the calculated patterns and the blue crosses indicate the origin of reciprocal space. Two different regions of reciprocal space have been circled for ease of comparison between the patterns (Color figure online)

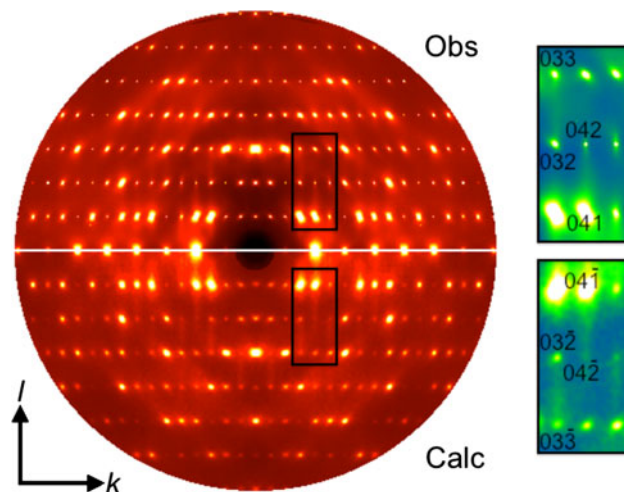


Fig. 8 The $0\ k\ l$ slice of reciprocal space from the X-ray diffuse scattering data (top half) at 322 K and the calculated diffuse scattering pattern (bottom half) from the combined orientational and displacive disorder model with a correlation coefficient of 0.6 for the G1 orientations between *b1* first neighbour types. The insets show the area around the diffuse streak between the (041) and (042) Bragg peaks

neighbour types could be mediated by the short hydrogen bond between G2 and G3 (see Fig. 6).

The thermal diffuse scattering also needs to be included in the model since the diffuse streaks due to the orientational SRO will be modulated by the thermal motions of the molecules. The calculated X-ray diffuse scattering pattern for the $0\ k\ l$ slice of reciprocal space from the combined SRO and thermal diffuse scattering model is shown in the lower half of Fig. 8. The correlation between *b1* neighbours is 0.6. The agreement with the X-ray data at 322 K both in terms of the broad thermal diffuse blobs centred on the Bragg peaks and the short occupancy-related streaks between Bragg peaks, is excellent.

Correlation coefficient for *b1* first neighbour types

To investigate the effect on the diffuse streaks of the strength of the correlations between *b1* neighbours, simulations were run with different values for the correlation coefficient. The real space distribution of the G1 orientations in the *bc* plane of the model crystal, as well as the corresponding calculated X-ray diffuse scattering in the $0\ k\ l$ slice of reciprocal space, are shown in Fig. 9. In real space as the correlation coefficient increases it causes the formation of linear domains of increasing length parallel to the ferroelectric *b* axis. In reciprocal space, increasing the correlation coefficient causes the intensity of the diffuse streaks to become stronger.

While, it is difficult to determine exactly what the correlation coefficient is between the G1 molecules in TGS

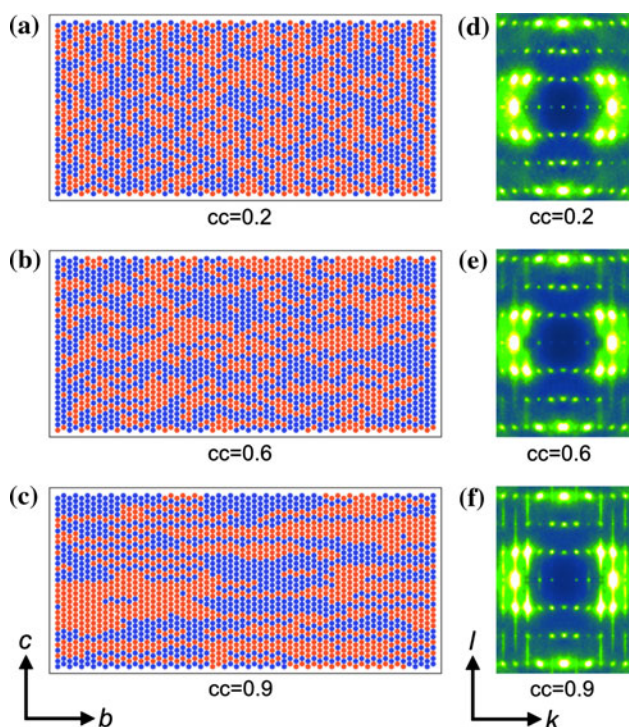


Fig. 9 The distribution of the G1 orientations (represented by the blue and orange circles) in the bc plane with a correlation coefficient (cc) between b1 first neighbour types of **a** 0.2, **b** 0.6 and **c** 0.9. The corresponding calculated X-ray diffuse scattering patterns for the 0 k l slice of reciprocal space are shown in parts **(d)** to **(f)**, respectively

from the model, a correlation coefficient of somewhere between 0.5 and 0.7 seems reasonable at T_C . Below 0.5, the diffuse streaks in the calculated patterns are barely visible, and above 0.7, they are unreasonably sharp (Fig. 10).

Dipole–dipole interactions between chains

These results strongly suggest that at temperatures above but close to T_C the G1 displacements couple via the short hydrogen bond between the G2 and G3 molecules. However, the ferroelectric state shows three-dimensional (3-d) ordering, so the question remains: is this 3-d ordering driven by hydrogen bonding or dipolar forces? It is likely that both contribute; as the 1-d chains lengthen, the weak lateral H-bonds will compound in their effect, and the local electrical polarisation will increase, resulting in a cooperative switch to 3-d order. The dipole energy was explored by testing which of four possible inter-chain configurations it preferred. Four different correlation structures between neighbouring chains along a and c were tested, as shown schematically in Fig. 11.

The potential energy of a pair of electric dipoles, \mathbf{p}_i and \mathbf{p}_j , is given by

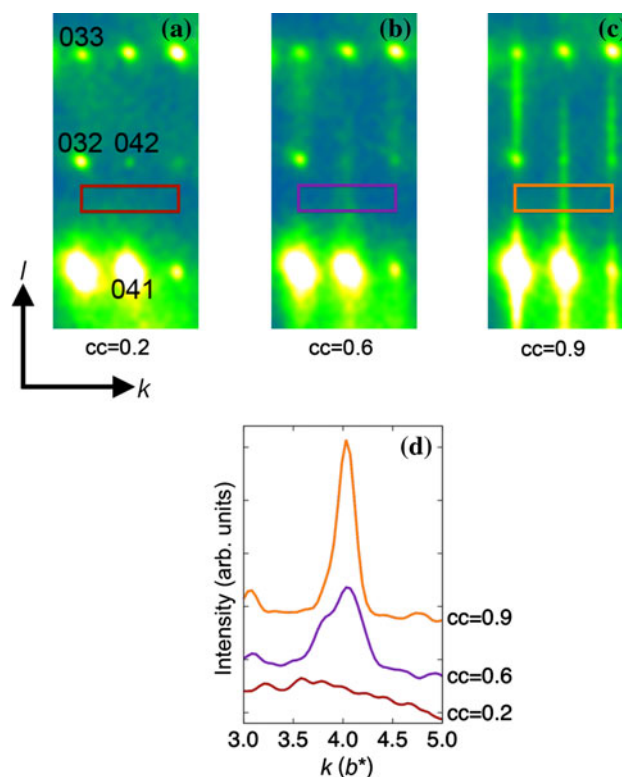


Fig. 10 The area around the diffuse streak between the (041) and (042) Bragg peaks in the 0 k l slice of reciprocal space calculated from the combined orientational and displacive disorder model with a correlation coefficient (cc) between b1 first neighbour types of **a** 0.2, **b** 0.6 and **c** 0.9. The plot profiles through the diffuse streak are shown in part **(d)** and have been vertically offset for clarity

$$U = \frac{\mathbf{p}_i \cdot \mathbf{p}_j}{r_{ij}^3} - \frac{3(\mathbf{p}_i \cdot \mathbf{r}_{ij})(\mathbf{p}_j \cdot \mathbf{r}_{ij})}{r_{ij}^5} \tag{2}$$

where \mathbf{r}_{ij} are the displacement vectors between the dipoles \mathbf{p}_i and \mathbf{p}_j [5]. The dipole interaction energy can be obtained by summing over all such interactions out to some cutoff radius.

The distribution of the dipole moments in the model was taken to be the same as the distribution of the disordered nitrogen atoms on G1. The dipole moments of the NH_3^+ groups were taken to be ± 1 , since it is the relative energies of the different correlation structures that is of interest. The orientations of the dipole moments within chains were assumed to be always parallel, which meant that the length of the chains along b in the model was infinite. The convergence of dipole interaction energies is known to be problematic [25], so the energy was calculated as a function of cutoff radius for all cases. The summation showed a strong preference for a 3-d parallel ordering of all moments.

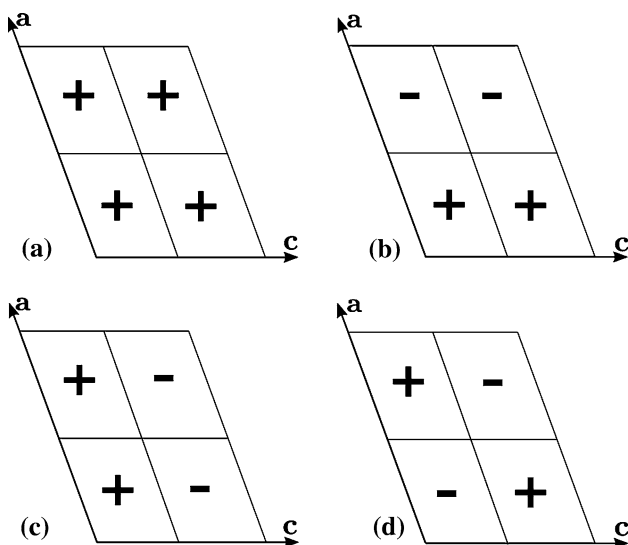


Fig. 11 Schematic of the different correlation structures along a and c between neighbouring chains of G1 molecules for which the dipole interaction energy (Eq. 2) was calculated: **a** parallel along a and c , **b** antiparallel along a and parallel along c , **c** parallel along a and antiparallel along c and **d** antiparallel along a and c . The view is looking down the b axis, so the zigzag chains of G1 molecules correlated via $b1$ neighbours, are coming out of the page. Chains with the G1 molecules positively and negatively oriented along the ferroelectric b axis are represented by the + and – signs, respectively

Conclusions

This study shows how the analysis of diffuse scattering can be used to build up a real-space picture of how molecular interactions lead to molecular ordering. As TGS is cooled the NH_3^+ groups form into chains which run in a zigzag parallel to the b axis. The growth of these chains appears related to the H-bonding network, and particularly interactions via the short hydrogen bond between the G2 and G3 molecules; that this initial ordering is driven by H-bonding and not dipolar interactions is supported by its strong anisotropy. It gives a 1-d correlation along b even though the dipolar interaction is 3-d in nature and neighbours in c are closer than those along the b and $b1$, and neighbours in a show a separation similar to neighbours along $b1$. Once the 1-d chains form, giving local regions of high polarisation, the dipolar interaction favours neighbouring chains to stack in a parallel fashion, such that when the ferroelectric state is obtained it shows full 3-d ordering. Hence, we suggest that this study gives a very reasonable real-space picture of the ferroelectric phase transition in TGS, including insight into the roles played by the different interactions. It also delivers a structural model, in the form of a model crystal, which successfully reproduces all the key features observed in the X-ray diffuse scattering, giving a comprehensive model of structure and mechanism in TGS.

Acknowledgements The authors gratefully acknowledge the Australian Institute for Nuclear Science and Engineering, the NCI National Facility and the Australian Research Council. Use of the Advanced Photon Source was supported by the U. S. Department of Energy, Office of Science, Office of Basic Energy Sciences, under Contract No. DE-AC02-06CH11357.

References

- Barabash RI, Ice GE, Turchi PEA (eds) (2009) Diffuse scattering and the fundamental properties of materials, 1st edn. Momentum Press, Highland Park
- Chan EJ, Welberry TR, Goossens DJ, Heerdegen AP (2010) J Appl Crystallogr 43:913
- Choudhury RR, Chitra R (2008) Pramana J Phys 71:911
- Choudhury RR, Chitra R (2009) J Phys Condens Mat 21:335901
- Choudhury RR, Chitra R, Ramanadham M (2003) J Phys Condens Mat 15:4641
- Choudhury RR, Chitra R, Sastry PU, Das A, Ramanadham M (2004) Pramana J Phys 63:107
- Estermann MA, Steurer W (1998) Phase Transit 67:165
- Fletcher SR, Keve ET, Skapski AC (1976) Ferroelectrics 14:775
- Fletcher SR, Keve ET, Skapski AC (1976) Ferroelectrics 14:789
- Fujii Y, Yamada Y (1971) J Phys Soc Jpn 30:1676
- Gonzalo JA (1966) Phys Rev 144:662
- Goossens DJ, Gutmann MJ (2009) Phys Rev Lett 102:015,505
- Goossens DJ, Heerdegen AP, Chan EJ, Welberry TR (2011) Metall Mater Trans A 42:23
- Hoshino S, Okaya Y, Pepinsky R (1959) Phys Rev 115:323
- Hudspeth JM, Goossens DJ (2012) J Cryst Growth 338:177
- Hudspeth JM, Goossens DJ, Gutmann MJ, Studer AJ (2013) Cryst Res Technol 48(3):169
- Jeffrey GA (1997) An introduction to hydrogen bonding. Oxford University Press, New York
- Kay MI (1977) Ferroelectrics 17:415
- Kay MI, Kleinberg R (1973) Ferroelectrics 5:45
- Keen DA, Gutmann MJ, Wilson CC (2006) J Appl Cryst 39:714
- Kikuta T, Hamatake D, Tamazaki T, Nakatani N (2007) Ferroelectrics 347:65
- Kikuta T, Tamazaki T, Nakatani N (2010) Ferroelectrics 403:111
- Lines ME, Glass AM (2001) Principles and applications of ferroelectrics and related materials. Oxford University Press, New York
- Neder RB, Proffen T (2008) Diffuse scattering and defect structure simulations. Oxford University Press, New York
- Pura B, Przedmojski J (1973) Phys Lett A 43:217
- Scheidegger S, Estermann MA, Steurer W (2000) J Appl Cryst 33:35
- Schneider CA, Rasband WS, Eliceiri KW (2012) Nat Methods (Oxford, UK) 9:671
- Schweika W (1998) Disordered alloys, diffuse scattering and Monte Carlo simulations. Springer, Berlin
- Shibuya I, Mitsui T (1961) J Phys Soc Jpn 16:479
- Tripadus V, Arangel D, Statescu M, Buchsteiner A (2008) Chem Phys 353:59
- Weber T, Estermann MA, Bürgi HB (2001) Acta Cryst B 57:579
- Welberry TR (2004) Diffuse X-ray Scattering and Models of Disorder. Oxford University Press, Oxford
- Welberry TR, Goossens DJ, David WIF, Gutmann MJ, Bull MJ, Heerdegen AP (2003) J Appl Cryst 36:1440
- Welberry TR, Goossens DJ, Heerdegen AP, Lee PL (2005) Z Krist 220:1052